Coexistence of phononic sixfold, fourfold, and threefold excitations in the ternary antimonide $Zr_3Ni_3Sb_4$

Mingmin Zhong,[1] Ying Liu,[2,*] Feng Zhou,[1] Minquan Kuang,[1] Tie Yang,[1] Xiaotian Wang,[1,†] and Gang Zhang[3,‡]

[1]*School of Physical Science and Technology, Southwest University, Chongqing 400715, China*

[2]*School of Materials Science and Engineering, Hebei University of Technology, Tianjin 300130, China*

[3]*Institute of High Performance Computing, Agency for Science, Technology and Research, Singapore 138632, Singapore*

(Received 22 February 2021; revised 24 June 2021; accepted 2 August 2021; published 11 August 2021)

Three-, four-, and sixfold excitations have significantly extended the subjects of condensed-matter physics. There is an urgent need for a realistic material that can have coexisting three-, four-, and sixfold excitations. However, these materials are uncommon because these excitations in electronic systems are usually broken by spin-orbit coupling (SOC) and are normally far from the Fermi level. Unlike the case in electronic systems, phonon systems with a negligible SOC effect, not constrained by the Pauli exclusion principle, provide a feasible platform to realize these excitations in a wide frequency range. Hence, in this work, we demonstrate by first-principles calculations and symmetry analysis that perfect three-, four-, sixfold excitations appear in the phonon dispersion rather than the band structures of $Zr_3Ni_3Sb_4$, which is a well-known indirect-gap semiconductor with an $Y_3Au_3Sb_4$-type structure. This material features a threefold-degenerate quadratic contact triple-point phonon, fourfold-degenerate Dirac point phonon, and sixfold degenerate point phonon. Moreover, these nodal point phonons are very robust to uniform strain. Two obvious phonon surface arcs of the (001) plane are extended in the whole Brillouin zone, which will facilitate their detection in future experimental studies. The current work provides an ideal model to investigate rich excitations in a single material.

DOI: 10.1103/PhysRevB.104.085118

I. INTRODUCTION

Condensed-matter systems [1] can host Dirac [2], Weyl [3], and Majorana fermions [4]. Dirac and Weyl fermions are well studied in many topological semimetals and topological metals [5–10], and their nodal points are four- and twofold-degenerate band-crossing points, respectively. Condensed-matter systems can also contain novel fermions without counterparts in high-energy physics, such as three-, six-, and eightfold excitations [11–15], due to fewer constraints placed by the space group symmetries. However, topological materials with unconventional six- and eightfold fermionic excitations under crystalline symmetry are rarely studied. In 2019, Schröter *et al.* [16] proposed that AlPt is a sixfold-degenerate nodal point topological semimetal and these sixfold-degenerate fermions can be regarded as a higher-spin extension of Weyl fermions. Such an unconventional excitation was also predicted in $PdSb_2$ [15], $PtBi_2$ [17], and $Li_{12}Mg_3Si_4$ [18]. In 2020, Zhang *et al.* predicted that eightfold fermionic excitations occur in high-quality $TaTe_4$ single crystals [14]. Unfortunately, these candidates with six- and eightfold fermionic excitations may have their own disadvantages. The sixfold fermionic excitations in $Li_{12}Mg_3Si_4$ [18] will be influenced by spin-orbit coupling (SOC); the unconventional quasiparticle excitations in $TaTe_4$ and AlPt [14,16] are far from the Fermi level, and $PdSb_2$ [15] hosts unclean electronic structures around the Fermi level.

Topological bosons [19–35] have been intensely studied and are also elementary excitations in condensed-matter systems. Phonons are the basic emergent boson of a crystalline lattice, and similar to fermionic electrons, topological phonons also exist in crystalline solids due to the crystal symmetry constraints. So far, twofold-degenerate Weyl phonons [23], along with threefold-degenerate nodal point phonons and fourfold-degenerate Dirac phonons [24,25], have been proposed in phonon systems. However, to the best of our knowledge, sixfold-degenerate phonons, which the maximal degeneracy in phonon systems, have not been predicted. In this work, first-principles calculations and symmetry analysis are used to study the topological phonons in a Zintl phase $Zr_3Ni_3Sb_4$ compound that was prepared by Wang *et al.* [36] via arc melting with an $Y_3Au_3Sb_4$-type structure. The structural models of a $Zr_3Ni_3Sb_4$ unit cell and a primitive cell are shown in Figs. 1(a) and 1(b), respectively. Zr, Ni, and Sb are located at 12a (3/8, 0, 1/4), 12b (7/8, 0, 1/4), and 16c (0.08207, 0.08207, 0.08207), respectively. It is well-known that $Zr_3Ni_3Sb_4$ is an indirect semiconductor, as shown by the electronic structures in Fig. 1(c). This compound has been widely used as a parent compound to fabricate a pair of *n*-type and *p*-type thermoelectric materials [37]. Here, we propose that $Zr_3Ni_3Sb_4$ hosts three kinds of phonon excitations, namely, a sixfold-degenerate nodal point phonon at the H point, a threefold-degenerate nodal point at the Γ point, and a fourfold-degenerate Dirac point at the P point. A detailed $k \cdot p$ model has also been constructed for these three points. The phonon surface states of the (001) plane are presented to demonstrate the Fermi arc states in $Zr_3Ni_3Sb_4$, and we also examine the dynamic stability and topological signatures under uniform strains.

*ying_liu@hebut.edu.cn

†xiaotianwang@swu.edu.cn

‡zhangg@ihpc.a-star.edu.sg

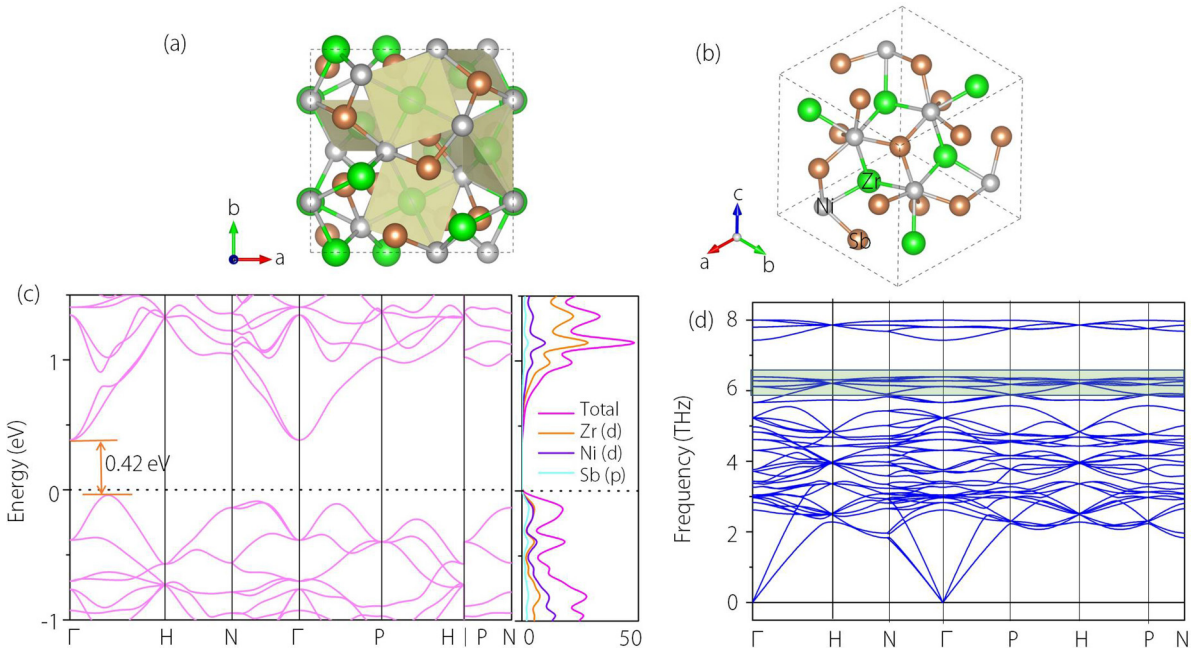

FIG. 1. (a) The unit cell and (b) primitive cell of $Zr_3Ni_3Sb_4$. The Zr, Ni, and Sb atoms are shown by green, gray, and brown balls, respectively. (c) The band structures and the density of states of the $Zr_3Ni_3Sb_4$ compound and (d) the calculated phonon dispersion of $Zr_3Ni_3Sb_4$.

II. METHODS

Density functional theory [38] was used to calculate the electronic structures, and we used the generalized gradient approximation Perdew-Burke-Ernzerhof [39] formalism for the exchange-correlation functional. The projector augmented-wave [40] method is used for the interactions between ions and valence electrons, and the energy cutoff is set to 500 eV. A Γ-centered k mesh of $10 \times 10 \times 10$ was used for Brillouin zone (BZ) sampling. The lattice dynamic calculations are performed to obtain the phonon dispersion of $Zr_3Ni_3Sb_4$ at equilibrium and strained lattice constants in the PHONOPY package [41] using density functional perturbation theory [42]. The topological behaviors of the (001) phonon surface states are calculated by constructing a Wannier tight-binding Hamiltonian of phonons [43]. Also, the Wannier charge center calculations were performed to obtain the Chern number of the phonons in $Zr_3Ni_3Sb_4$.

III. RESULTS AND DISCUSSION

The crystal structure of $Zr_3Ni_3Sb_4$ was totally relaxed, and the calculated lattice constants were found to be $a = b = c = 9.1346$ Å, which agrees well with the experimental values of $a = b = c = 9.066$ Å [36]. The primitive cell of $Zr_3Ni_3Sb_4$ shown in Fig. 1(b) was used to calculate the band structure. Cubic-type $Zr_3Ni_3Sb_4$ belongs to space group $I\bar{4}3d$ with a space group number of 220. The three-dimensional (3D) BZ is shown in Fig. 2(a), and the band structures and the density of states are shown in Fig. 1(c). Obviously, $Zr_3Ni_3Sb_4$ is a semiconductor with an indirect band gap of 0.42 eV.

Figure 1(d) shows the calculated phonon spectra of $Zr_3Ni_3Sb_4$ along the high-symmetry points Γ-*H*-*N*-Γ-*P*-*H*-*P*-*N* as depicted in Fig. 2(a). It can be seen that no acoustic-optical branch gap appears in the phonon spectra and $Zr_3Ni_3Sb_4$ is dynamically stable due to the absence of imaginary frequencies. We observe rich types of nodal point phonons in the 6.10–6.25 THz region, as shown in Fig. 2(b). A series of phonon band-crossing points appears in this region as a sixfold-degenerate point (SFP) at H, a quadratic contact triple point (QCTP) at Γ, and a fourfold-degenerate Dirac point (DP) at P, and because these are phonons, we do not need to consider the Pauli exclusion principle as required in electronic systems. Therefore, these rich three-, four-, and sixfold-degenerate phonons can be realized in a wide range of phonon frequencies. To our knowledge, the QCTP phonons and the SFP phonons have not been considered to date.

We have studied these excitations individually. As shown in Fig. 2(c), the DP at the P point with a frequency of ∼6.18 THz is formed by a doubly degenerate phonon band and two nondegenerate phonon bands. These DPs in Fig. 2(c) with a graphenelike linear phonon band dispersion belong to type I nodal points, as described in Ref. [44]. The topological phonons at the P point can be confirmed on the basis of an effective model around P. The little group at this point is C_{3v}, which is generated by four independent operations, namely, C_{32}^{+}, C_{2y}, C_{2x}, and S_{4x}^{+}. The irreducible representation (IRR) at this point is Γ_3. As a consequence, the generators based on this representation are given by

$$C^{+}_{3,\bar{1}\bar{1}1} = \frac{1}{2\sqrt{2}} \begin{pmatrix} (-1)^{1/4} & -(-1)^{3/4} & \sqrt{3} & -i\sqrt{3} \\ (-1)^{1/4} & (-1)^{3/4} & \sqrt{3} & i\sqrt{3} \\ -i\sqrt{3} & -\sqrt{3} & (-1)^{1/4} & -(-1)^{3/4} \\ -i\sqrt{3} & \sqrt{3} & (-1)^{1/4} & (-1)^{3/4} \end{pmatrix},$$

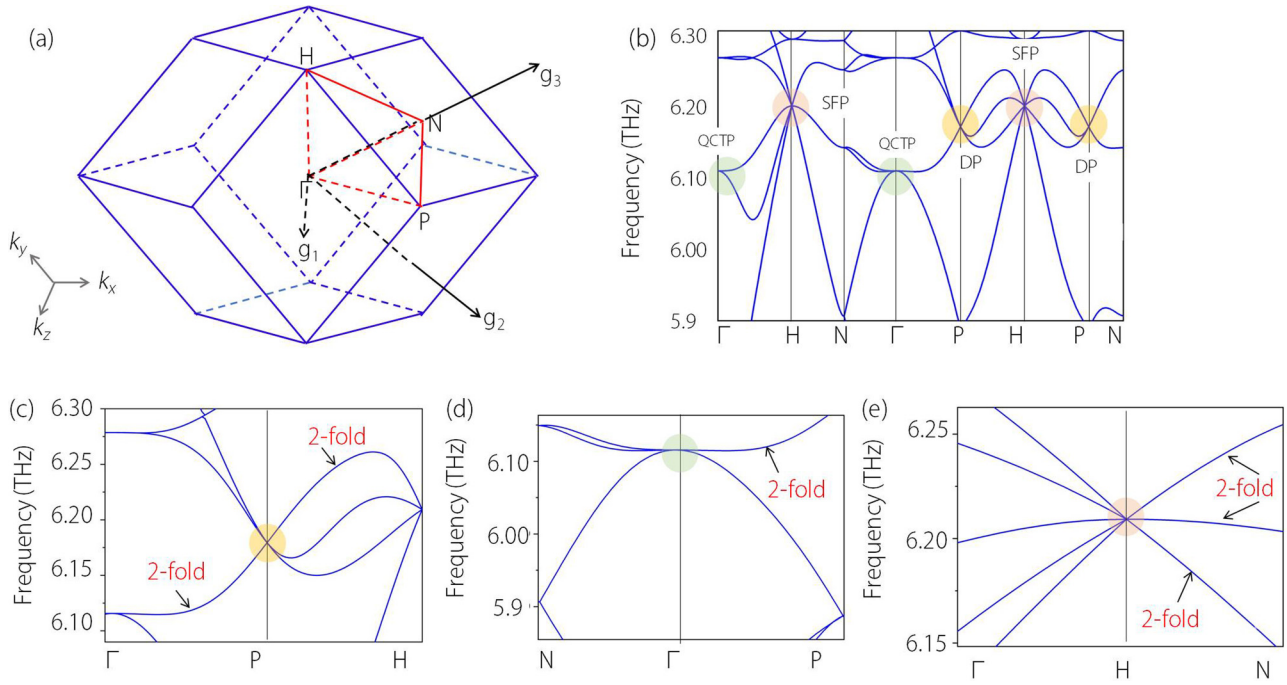

FIG. 2. (a) Three-dimensional coordinate system of the BZ and some high-symmetry points. (b) Enlarged frequencies of $Zr_3Ni_3Sb_4$ with rich nodal point phonons. The SFP, QCTP, and DP at H, Γ, and P are highlighted in red, green, and yellow. (c)–(e) The phonon band-crossing points at the P, Γ, and H points, respectively.

$$C_{2y} = \begin{pmatrix} 0 & 1 & 0 & 0 \\ 1 & 0 & 0 & 0 \\ 0 & 0 & 0 & 1 \\ 0 & 0 & 1 & 0 \end{pmatrix},$$

$$C_{2x} = \begin{pmatrix} 1 & 0 & 0 & 0 \\ 0 & -1 & 0 & 0 \\ 0 & 0 & 1 & 0 \\ 0 & 0 & 0 & -1 \end{pmatrix}, S_{4x}^{+} = \begin{pmatrix} 1 & 0 & 0 & 0 \\ 0 & i & 0 & 0 \\ 0 & 0 & -1 & 0 \\ 0 & 0 & 0 & -i \end{pmatrix}.$$

Here, we should point out that the P point is not the time reversal invariant momentum. Therefore, the effective Hamiltonian is required to be invariant under these spatial symmetries,

$$\mathcal{R}(G)H\left(G^{-1}k\right)\mathcal{R}^{-1}(G) = H(k), \tag{1}$$

where G stands for the generator and it runs over all generators and $\mathcal{R}$ is the corresponding matrix form. Hence, the effective Hamiltonian can be written in a general form,

$$H_{\mathrm{DP}}(\boldsymbol{k}) = \begin{bmatrix} h_{11}(\boldsymbol{k}) & h_{12}(\boldsymbol{k}) \\ h_{21}(\boldsymbol{k}) & h_{22}(\boldsymbol{k}) \end{bmatrix}, \tag{2}$$

where each $h_{\mathrm{ij}}(\boldsymbol{k})$ is a 2×2 matrix as described by

$$h_{11}(\boldsymbol{k}) = -h_{22}(\boldsymbol{k}) = \begin{bmatrix} 0 & vk_{-} \\ vk_{+} & 0 \end{bmatrix}, \tag{3}$$

$$h_{12}(\boldsymbol{k}) = h_{21}^{*}(\boldsymbol{k}) = \begin{bmatrix} \beta k_z & \alpha k_{+} \\ \alpha^{*} k_{-} & -\beta k_z \end{bmatrix}. \tag{4}$$

Here, v is real, while α and β are imaginary parameters. It can be seen that a degenerate point features a linear dispersion in any direction in k space, and since the P point is invariant under mirror $\widetilde{M}_{110}$, it carries a zero Chern number.

Figure 2(d) shows the QCTP phonon at the Γ point with a frequency of ∼6.11 THz. The phonon bands at Γ exhibit a quadratic dispersion [45] along N-Γ-P paths as opposed to the linear dispersion at P. There is one nondegenerate phonon band and one twofold-degenerate phonon band along the Γ-P direction. However, this band splits into two single ones along the N-Γ path. Although threefold-degenerate nodal point fermions have been widely proposed in electronic systems [46–50], such as APd_3 (A = Pb, Sn) [46], nonsymmorphic Ba_3Si_4 [49], Li_2NaN [50], and TiB_2 [48], the SOC will usually induce a gap to the band-crossing point and thus break the threefold-degenerate nodal point fermions. The QCTP in a phononic system can be viewed as an ideal threefold-degenerate nodal point because phonon systems have a negligible SOC effect. To capture the physics of the QCTP at the Γ point, an effective Hamiltonian can be derived. The little group at the Γ point is T_d, which is generated by a threefold rotation along the [111] direction, two twofold rotations along the z and y axes, and mirror symmetry along the $[1\bar{1}0]$ direction. At the Γ point, there exists a 3D IRR, i.e., Γ_4. According to this irreducible representation, the generators take the following form:

$$C_{31}^{-} = \begin{pmatrix} 0 & 0 & 1 \\ 1 & 0 & 0 \\ 0 & 1 & 0 \end{pmatrix}, \quad C_{2y} = \begin{pmatrix} 1 & 0 & 0 \\ 0 & -1 & 0 \\ 0 & 0 & -1 \end{pmatrix},$$

$$C_{2z} = \begin{pmatrix} -1 & 0 & 0 \\ 0 & -1 & 0 \\ 0 & 0 & 1 \end{pmatrix},$$

$$M_{1\bar{1}0} = \begin{pmatrix} 0 & 1 & 0 \\ 1 & 0 & 0 \\ 0 & 0 & 1 \end{pmatrix}, \quad \mathcal{T} = I_{3\times 3}\mathcal{K}.$$

Here, $\mathcal{K}$ is the complex conjugation. According to Eq. (1), the effective model could be written as

$$H_{\mathrm{QCTP}}(\boldsymbol{k}) = \begin{bmatrix} A_1k_x^2 + A_2\left(k_y^2 + k_z^2\right) & Bk_xk_y & Bk_xk_z \\ Bk_xk_y & A_1k_y^2 + A_2\left(k_x^2 + k_z^2\right) & Bk_yk_z \\ Bk_xk_z & Bk_yk_z & A_1k_z^2 + A_2\left(k_y^2 + k_x^2\right) \end{bmatrix}. \tag{5}$$

Here, parameters A_1, A_2, and B are real parameters. Such a QCTP has zero topological charge due to the glide mirror, and such a QCTP is a typical topological state that occurs only in spinless systems.

The sixfold-degenerate nodal point at the H point has a frequency of ~6.207 THz. As shown in Fig. 2(e), three doubly degenerate phonon bands merge at the H point along the H-N direction to form a sixfold-degenerate phonon band crossing with linear dispersion. The sixfold-degenerate nodal point phonons are the maximum degeneracy in phonon systems, and these excitations in spin-free systems are not well studied. This work shows a realistic material to study the unconventional sixfold-degenerate nodal point phonons. We construct a Hamiltonian of the phonon system around the H point to uncover the physical origin of the sixfold excitations.

The small group around the H point belongs to T_d, which is generated by a reflection fourfold rotation (S_{4x}), a glide mirror (M_{110}), and a threefold rotation (C_{33}^-), and there exist two 3D IRRs, namely, Γ_4 and Γ_5. Therefore, the corresponding generating elements could take the following forms:

$$S_{4x} = \tau_z \otimes (iW), \quad M_{110} = \tau_z \otimes (iX),$$

$$C_{33}^- = \tau_0 \otimes A, \quad \mathcal{T} = I_{6\times6}\mathcal{K}.$$

Here, τ is the Pauli matrix, and

$$W = \begin{pmatrix} 0 & 1 & 0 \\ -1 & 0 & 0 \\ 0 & 0 & 1 \end{pmatrix}, \quad X = \begin{pmatrix} 1 & 0 & 0 \\ 0 & 0 & 1 \\ 0 & 1 & 0 \end{pmatrix},$$

$$A = \begin{pmatrix} 0 & 0 & 1 \\ 1 & 0 & 0 \\ 0 & 1 & 0 \end{pmatrix}.$$

Required by these generators, the effective model can be written as

$$H(\boldsymbol{k}) = \begin{bmatrix} h_{11}(\boldsymbol{k}) & h_{12}(\boldsymbol{k}) \\ h_{21}(\boldsymbol{k}) & h_{22}(\boldsymbol{k}) \end{bmatrix} \tag{6}$$

based on Eq. (1). Here, $\boldsymbol{k}$ is measured from the H point, and each $h_{ij}(\boldsymbol{k})$ is a 3×3 matrix as described below. In detail,

$$h_{11}(\boldsymbol{k}) = -h_{22}(\boldsymbol{k}) = \gamma \boldsymbol{k} \cdot \boldsymbol{S}, \tag{7}$$

where $\boldsymbol{S}$ is the angular momentum for a spin-1 particle that satisfies

$$[S_i, S_j] = i\epsilon_{ijk}S_k. \tag{8}$$

There are two spin-1 particles of opposite helicity in the diagonal positions, and

$$h_{12}(\boldsymbol{k}) = h_{21}^*(\boldsymbol{k}) = \begin{bmatrix} 0 & -\gamma_1 k_x & \gamma_2 k_y \\ -\gamma_2 k_x & 0 & \gamma_1 k_z \\ \gamma_1 k_y & \gamma_2 k_z & 0 \end{bmatrix} \tag{9}$$

if we consider the limitations $|\gamma| \gg |\gamma_1|$ and $|\gamma| \gg |\gamma_2|$ in Eq. (9). Such a limitation does not change the topology at the H point. This sixfold-degenerate point is a composition of two decoupled spin-1 particles that carries zero topological charge. The degenerate point is still gapless when taking the off-diagonal terms into consideration, and no topological phase transition happens. Therefore, the sixfold-degenerate point at that H point has a Chern number of zero. We also calculate the Chern number of the phonons in $Zr_3Ni_3Sb_4$ based on the Wannier charge center methods [43], and we find the Chern number SFP at the H point is equal to zero, agreeing well with results based on our symmetry analysis.

A phonon tight-binding Hamiltonian as implemented in the WANNIERTOOLS package [43] was used to calculate the phonon surface states of $Zr_3Ni_3Sb_4$ to further our understanding of the topological features at these multifold-degenerate points. The results of (001) phonon surface states and the corresponding isofrequency surfaces for $Zr_3Ni_3Sb_4$ at $E1 = 6.21$ THz and $E2 = 6.10$ THz are presented in Fig. 3. The SFP, DP, and QCTP are shown by red, yellow, and green circles, respectively, in Fig. 3(a). There are, indeed, two phonon surface arcs [51,52] emanating from these nodal points. These two phonon surface states around the SFP, DP, and QCTP are marked by red, black, and yellow arrows, respectively. It is well-known that clear surface states can facilitate their detection in future

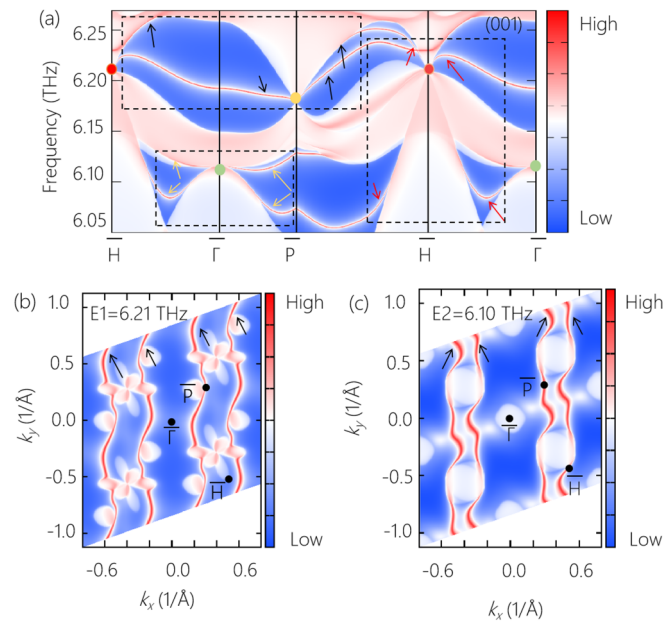

FIG. 3. (a) The phonon surface states of the (001) plane. The SFP, DP, and QCTP are marked by red, yellow, and green circles. The phonon surface arc states around the SFP, DP, and QCTP are highlighted by red, black, and yellow arrows. The isofrequency surfaces at (b) $E1 = 6.21$ THz and (c) $E2 = 6.10$ THz.

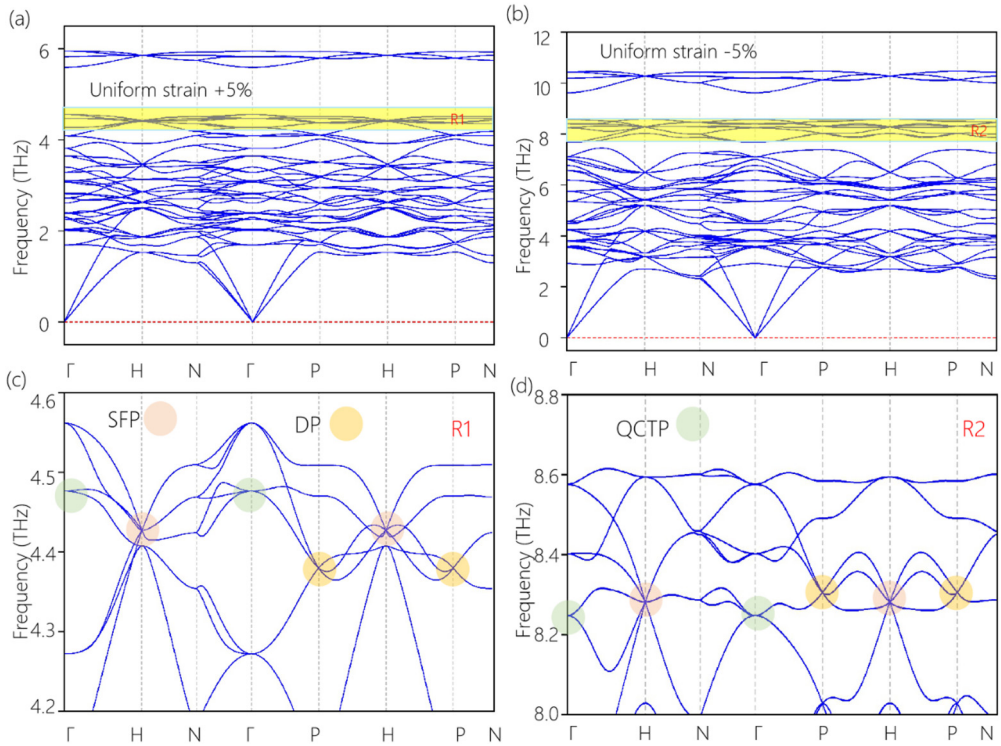

FIG. 4. The phonon dispersion spectra of $Zr_3Ni_3Sb_4$ at (a) +5% uniform strain and (b) −5% uniform strains. (c) and (d) Enlarged plots of (a) and (b). The SFP, QCTP, and DP are highlighted by different colored circles in (c) and (d).

experiments. These phonon surface states are extended in the whole BZ on the (001) surface, as shown in Figs. 3(b) and 3(c). The reason may be that the QCTP at Γ is located at the center of the BZ, while the SFP and DP at H and P are at the corner of the BZ and these phonon surface states will connect these projections and extend over the whole BZ of the (001) side surface [see the black arrows in Figs. 3(b) and 3(c)].

These symmetry-protected excitations are very robust to uniform strains. Figures 4(a) and 4(b) show the calculated phonon dispersion of $Zr_3Ni_3Sb_4$ under ±5% uniform strains, and it is dynamically stable in this range. The SFP, QCTP, and DP phonons are still maintained in this region. The enlarged phonon dispersions of the highlighted parts of Figs. 4(a) and 4(b) are shown in Figs. 4(c) and 4(d), respectively. However, the regions of these multifold-degenerate points are reduced and increased by ∼2 THz under the −5% and +5% uniform strains, respectively.

IV. CONCLUSIONS AND REMARKS

In summary, we propose $Zr_3Ni_3Sb_4$ is an existing material with three-, four-, and sixfold excitations. The SFP, DP, and QCTP phonons at the H, P, and Γ points are in frequency regions of 6.10–6.25 THz, and $Zr_3Ni_3Sb_4$ can be viewed as an ideal candidate for investigating unconventional quasiparticles in bulk materials. Moreover, $Zr_3Ni_3Sb_4$ has phonon surface arcs that extend the entire BZ of the side surface. These multifold-degenerate points are maintained in phonon dispersion with ±5% uniform strains. Without SOC and the restriction of the Pauli exclusion principle, $Zr_3Ni_3Sb_4$ is an ideal test case to study unconventional quasiparticles, and we expect it will be confirmed experimentally.

Before closing this paper, we note the following: (i) $Zr_3Ni_3Sb_4$ does not host net Chern number; there is no guarantee of topologically protected surface states in the strictest sense. Similar to the sixfold excitation in $Li_{12}Mg_3Si_4$ material [18], the three-, four-, and sixfold excitations in $Zr_3Ni_3Sb_4$ will lead to trivial "Fermi arc" states on the surfaces, although they are not topologically protected. (ii) Topological phases [53] contain a topologically nontrivial phase and a topologically trivial phase. Because the SFP, DP, and QCTP phonons at the H, P, and Γ points have zero topological charge, they belong to topologically trivial phonons. (iii) With the effect of SOC, the phonon dispersion of $Zr_3Ni_3Sb_4$ at the ground state along Γ-H-N-Γ-P-H-P-N paths is shown in Fig. S1 (see the Supplemental Material (SM) [54]). From Fig. S1, one finds the phonon dispersion seems to be totally unaffected by the SOC effect. (iv) Compared to two- and fourfold cases, the three- and sixfold degeneracies of phonon band crossings are particularly intriguing since there are no counterparts in high-energy physics due to Poincaré symmetry constraints. Moreover, compared to threefold cases, the sixfold excitations have attracted considerable interest owing to the presence of the maximum degeneracy in bosonic systems. Recent discoveries promptly confirmed the existence of threefold- and sixfold-degenerate symmetry-protected nodal points in topological materials [55,56], which can endow these materials with unusual physical properties, like anomalous negative magnetoresistance [54] and hinge arc states [18]. Hence, if three-, four-, and sixfold excitations coexisted in one single solid-state material, the study of the entanglement among these excitations would be very interesting. (v) The SFP, DP, and QCTP phonons at the H, P, and Γ points are symmetry-enforced points [57]. Hence, these nodal point phonons may

occur in different frequency ranges. Note that obvious SFP, DP, and QCTP phonons can also be observed around the 7.8 THz region (see Fig. S2 in the SM). (vi) Last, but not least, phononic band structures are perfect playgrounds to diminish the detrimental effects of SOC and the Pauli exclusion principle. However, electronic band structures have their unique advantages; for example, they are perfect playgrounds to investigate the role of correlations in higher-order excitations [58].

[1] P. B. Pal, Am. J. Phys. **79**, 485 (2011).
[2] S. Y. Zhou, G. H. Gweon, J. Graf, A. V. Fedorov, C. D. Spataru, R. D. Diehl, and A. Lanzara, Nat. Phys. **2**, 595 (2006).
[3] K. Kuroda, T. Tomita, M. T. Suzuki, C. Bareille, A. A. Nugroho, P. Goswami, and S. Nakatsuji, Nat. Mater. **16**, 1090 (2017).
[4] S. R. Elliott and M. Franz, Rev. Mod. Phys. **87**, 137 (2015).
[5] S. M. Young and C. L. Kane, Phys. Rev. Lett. **115**, 126803 (2015).
[6] N. P. Armitage, E. J. Mele, and A. Vishwanath, Rev. Mod. Phys. **90**, 015001 (2018).
[7] B. J. Wieder, Y. Kim, A. M. Rappe, and C. L. Kane, Phys. Rev. Lett. **116**, 186402 (2016).
[8] T. R. Chang, S. Y. Xu, D. S. Sanchez, W. F. Tsai, S. M. Huang, G. Chang, C. H. Hsu, G. Bian, I. Belopolski, Z. M. Yu, S. A. Yang, T. Neupert, H. T. Jeng, H. Lin, and M. Z. Hasan, Phys. Rev. Lett. **119**, 026404 (2017).
[9] S. Kobayashi and M. Sato, Phys. Rev. Lett. **115**, 187001 (2015).
[10] B. Q. Lv, H. M. Weng, B. B. Fu, X. P. Wang, H. Miao, J. Ma, P. Richard, X. C. Huang, L. X. Zhao, G. F. Chen, Z. Fang, X. Dai, T. Qian, and H. Ding, Phys. Rev. X **5**, 031013 (2015).
[11] C. K. Barman, C. Mondal, B. Pathak, and A. Alam, Phys. Rev. B **99**, 045144 (2019).
[12] H. Weng, C. Fang, Z. Fang, and X. Dai, Phys. Rev. B **93**, 241202(R) (2016).
[13] Z. Zhu, G. W. Winkler, Q. S. Wu, J. Li, and A. A. Soluyanov, Phys. Rev. X **6**, 031003 (2016).
[14] X. Zhang *et al.* Phys. Rev. B **102**, 035125 (2020).
[15] Z. P. Sun, C. Q. Hua, X. L. Liu, Z. T. Liu, M. Ye, S. Qiao, Z. H. Liu, J. S. Liu, Y. F. Guo, Y. H. Lu, and D. W. Shen, Phys. Rev. B **101**, 155114 (2020).
[16] N. B. Schröter, D. Pei, M. G. Vergniory, Y. Sun, K. Manna, F. De Juan, and Y. Chen, Nat. Phys. **15**, 759 (2019).
[17] S. Thirupathaiah, Y. S. Kushnirenk, K. Koepernik, B. R. Piening, B. Buechner, S. Aswartham, and I. C. Fulga, SciPost Phys. **10**, 004 (2021).
[18] S. Nie, B. A. Bernevig, and Z. Wang, Phys. Rev. Res. **3**, L012028 (2021).
[19] B. Zheng, B. Xia, R. Wang, Z. Chen, J. Zhao, Y. Zhao, and H. Xu, Phys. Rev. B **101**, 100303(R) (2020).
[20] F. D. M. Haldane and S. Raghu, Phys. Rev. Lett. **100**, 013904(R) (2008).
[21] R. Süsstrunk and S. D. Huber, Science **349**, 47 (2015).
[22] F. Liu, H. Y. Deng, and K. Wakabayashi, Phys. Rev. B **97**, 035442 (2018).
[23] T. Zhang, Z. Song, A. Alexandradinata, H. Weng, C. Fang, L. Lu, and Z. Fang, Phys. Rev. Lett. **120**, 016401 (2018).
[24] Y. Jin, R. Wang, and H. Xu, Nano Lett. **18**, 7755 (2018).
[25] S. Singh, Q. S. Wu, C. Yue, A. H. Romero, and A. A. Soluyanov, Phys. Rev. Mater. **2**, 114204 (2018).
[26] O. Stenull, C. L. Kane, and T. C. Lubensky, Phys. Rev. Lett. **117**, 068001 (2016).
[27] C. L. Kane and T. C. Lubensky, Nat. Phys. **10**, 39 (2014).
[28] Y. J. Jin, Z. J. Chen, B. W. Xia, Y. J. Zhao, R. Wang, and H. Xu, Phys. Rev. B **98**, 220103(R) (2018).
[29] S. H. Mousavi, A. B. Khanikaev, and Z. Wang, Nat. Commun. **6**, 8682 (2015).
[30] Y. Liu, Y. Xu, S. C. Zhang, and W. Duan, Phys. Rev. B **96**, 064106 (2017).
[31] Y. Liu, Y. Xu, and W. Duan, Natl. Sci. Rev. **5**, 314 (2018).
[32] L. Zhang and Q. Niu, Phys. Rev. Lett. **115**, 115502 (2015).
[33] L. Lu, L. Fu, J. D. Joannopoulos, and M. Soljačić, Nat. Photonics **7**, 294 (2013).
[34] F. Li, X. Huang, J. Lu, J. Ma, and Z. Liu, Nat. Phys. **14**, 30 (2018).
[35] M. Mori, A. Spencer-Smith, O. P. Sushkov, and S. Maekawa, Phys. Rev. Lett. **113**, 265901 (2014).
[36] M. Wang, R. McDonald, and A. Mar, Inorg. Chem. **38**, 3435 (1999).
[37] Z. Liu, J. Mao, S. Peng, B. Zhou, W. Gao, J. Sui, and Z. Ren, Mater. Today Phys. **2**, 54 (2017).
[38] R. G. Parr, Annu. Rev. Phys. Chem. **34**, 631 (1983).
[39] J. P. Perdew, K. Burke, and M. Ernzerhof, Phys. Rev. Lett. **80**, 891 (1998).
[40] P. E. Blochl, Phys. Rev. B **50**, 17953 (1994).
[41] A. Togo and I. Tanaka, Scr. Mater. **108**, 1 (2015).
[42] S. Baroni, S. De Gironcoli, A. Dal Corso, and P. Giannozzi, Rev. Mod. Phys. **73**, 515 (2001).
[43] Q. Wu, S. Zhang, H. F. Song, M. Troyer, and A. A. Soluyanov, Comput. Phys. Commun. **224**, 405 (2018).
[44] S. Li, Z. M. Yu, Y. Liu, S. Guan, S. S. Wang, X. Zhang, Y. Yao, and S. A. Yang, Phys. Rev. B **96**, 081106(R) (2017).
[45] Z. Zhu, Y. Liu, Z. M. Yu, S. S. Wang, Y. X. Zhao, Y. Feng, X. L. Sheng, and S. A. Yang, Phys. Rev. B **98**, 125104 (2018).
[46] K. H. Ahn, W. E. Pickett, and K. W. Lee, Phys. Rev. B **98**, 035130 (2018).
[47] H. Yang, J. Yu, S. S. P. Parkin, C. Felser, C. X. Liu, and B. Yan, Phys. Rev. Lett. **119**, 136401 (2017).
[48] X. Feng, C. Yue, Z. Song, Q. S. Wu, and B. Wen, Phys. Rev. Mater. **2**, 014202 (2018).
[49] J. Cai, Y. Xie, P. Y. Chang, H. S. Kim, and Y. Chen, Phys. Chem. Chem. Phys. **20**, 21177 (2018).
[50] L. Jin, X. Zhang, X. Dai, H. Liu, G. Chen, and G. Liu, J. Mater. Chem. C **7**, 1316 (2019).
[51] Z. Huang, Z. Chen, B. Zheng, and H. Xu, npj Comput. Mater. **6**, 87 (2020).
[52] B. W. Xia, R. Wang, Z. J. Chen, Y. J. Zhao, and H. Xu, Phys. Rev. Lett. **123**, 065501 (2019).
[53] F. Liu and K. Wakabayashi, Phys. Rev. Lett. **118**, 076803 (2017).
[54] See Supplemental Material at http://link.aps.org/supplemental/10.1103/PhysRevB.104.085118 for the phonon dispersion of

$Zr_3Ni_3Sb_4$ with the SOC effect and enlarged frequencies of $Zr_3Ni_3Sb_4$ around 7.8 THz.

[55] B. Bradlyn, J. Cano, Z. Wang, M. G. Vergniory, C. Felser, R. J. Cava, and B. A. Bernevig, Science **353**, aaf5037 (2016).

[56] N. Kumar, M. Yao, J. Nayak, M. G. Vergniory, J. Bannies, Z. Wang, N. B. M. Schroter, S. V. N. L. Muchler, W. Shi, E. D. L. Rienks, J. L. Manes, C. Shekhar, S. S. P. Parkin, J. Fink, G. H. Fecher, Y. Sun, B. A. Bernevig, and C. Felser, Adv. Mater. **32**, 1906046 (2020).

[57] Z. M. Yu, Z. Zhang, G. B. Liu, W. Wu, X. P. Li, R. W. Zhang, S. A. Yang, and Y. Yao, arXiv:2102.01517.

[58] D. Di Sante, A. Hausoel, P. Barone, J. M. Tomczak, G. Sangiovanni, and R. Thomale, Phys. Rev. B **96**, 121106(R) (2017).